International Journal of Heat and Mass Transfer 161 (2020) 120312

Contents lists available at ScienceDirect

International Journal of Heat and Mass Transfer

journal homepage: www.elsevier.com/locate/hmt

Ultra-low pressure drop membrane-based heat sink with 1000 W/cm^2 cooling capacity and 100% exit vapor quality

Morteza Alipanah, Saeed Moghaddam*

Mechanical and Aerospace Engineering, University of Florida, Gainesville, FL 32611, United States

ARTICLE INFO

Article history:
Received 10 May 2020
Revised 8 August 2020
Accepted 8 August 2020
Available online 22 August 2020

ABSTRACT

This paper presents the most recent progress on advancing the membrane-based heat sink (MHS) science. A model developed to predict the MHS performance suggested that the membrane permeability limited the critical heat flux (CHF). The new generation MHS discussed here benefits from a newly developed membrane with 7 times higher permeability compared to the membrane used in the previous generation MHS. Experimental studies were conducted on a heat sink with a heater surface area of 0.7 × 0.7 cm^2. The results confirmed that a higher membrane permeability substantially increases the CHF of surface structures with enhanced wickability and surface area ratio (A_r) at low pressure drops. A maximum CHF of about 1000 W/cm^2 was achieved on a surface with A_r = 3.45 at a supplied liquid pressure of only 4 kPa, 2.5 times higher than the CHF reached with the low permeability membrane used in the first generation MHS. The new membrane enhanced the heat transfer coefficient at low supplied liquid pressures but substantially less than the 1.8 MW/m^2 K reached at the highest pressure (i.e. 20 kPa). This low pressure drop along with a heat sink exit vapor quality of 100% resulted in an extremely low pumping power. The ratio of CHF versus the theoretical pumping power is 1–2 orders of magnitude higher than that of the other two-phase heat sinks reported in the literature.

1. Introduction

The ever-increasing generation of waste heat has become an impediment to development of the next generation electronics and energy devices such as microprocessors, solid-state lasers, and power electronics. Single phase liquid cooling, a once innovative thermal management technique a decade ago, can no longer meet the needs of emerging devices that can generate die-level waste heat rates on the order of 1000 W/cm^2 [1–4]. Due to such a high heat generation rate, to maintain an acceptable streamwise temperature rise, a single-phase liquid cooling system must operate at high flow rates, resulting in a high pressure drop and pumping power. To overcome these challenges, cooling by boiling heat transfer process is being pursued. The bubble ebullition process in boiling triggers a set of heat and mass transfer events such as microconvection near the heater surface and rapid formation and evaporation of ultra-thin liquid films that can dissipate extremely high heat rates [5,6]. However, the efforts to take advantage of this potential have been hampered by a limited understanding of a phenomena commonly known as the critical heat flux (CHF).

After seminal studies of Nukiyama [7] on identifying the CHF, pioneering scientists have attempted to understand the physical nature of CHF and enhance its technical limit. Early studies [8–11] suggested that hydrodynamic aspects of nucleate pool boiling are similar to the process of a gas bubbling into a liquid through a perforated plate, and the hydrodynamic instability associated with this process, when the flow of gas reaches a critical limit, resembles that of CHF. Kutateladze [12] noted that close to CHF, the liquid streams returning to the surface in between vapor columns leaving the surface are interrupted, and concluded that the crisis in the boiling process is a hydrodynamic phenomenon. Kutateladze [12] and Zuber [11] developed models that predicted CHF values of 153 and 127 W/cm^2, respectively, for boiling of saturated water at 1 atm on a planar surface.

Over the following decades, numerous studies were conducted on CHF to both understand its cause and increase its value. The efforts have been primarily focused on engineering the surface [13]. CHF values well below and above the Kutateladze and Zuber (K–Z) hydrodynamics limit have been observed. Moissis and Berenson [14] and Bui and Dhir [15] established that hydrophilic surfaces have a higher CHF than hydrophobic ones. Conversely, Jo et al. [16] reduced the CHF by ~5× relative to Zuber's predictions using hydrophobic coatings. The effect of wettability on CHF has been modeled by Kandlikar [17] who postulated that CHF occurs

* Corresponding author.
E-mail address: saeedmog@ufl.edu (S. Moghaddam).

https://doi.org/10.1016/j.ijheatmasstransfer.2020.120312
0017-9310/

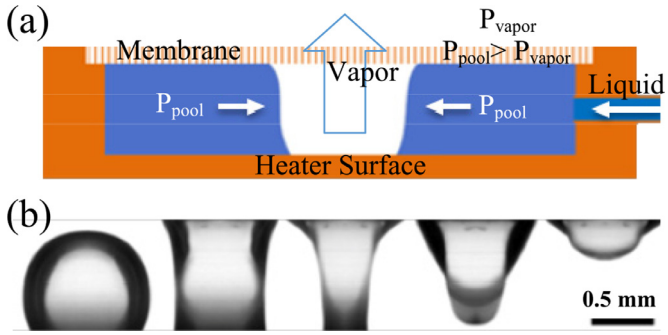

Fig. 1. (a) Schematic cross-section of the membrane-based heat sink (not to scale) and (b) visualization of an air bubble extraction process from a pool of water constrained by a hydrophobic membrane in an adiabatic test.

when the momentum flux caused by evaporation at the contact line overcomes forces responsible for heater rewetting, leading to CHF. This was modeled expressing the K–Z limit as a function of the wetting angle.

Recent studies on well-defined microfabricated structures can also be credited for identifying the effect of another surface parameter on CHF. Notably, Ahn et al. [18] differentiated the capability of a surface to spread a liquid from just reducing its contact angle. They found this effect responsible for a marked uptake in CHF enhancement ratio relative to Kandlikar's model [17]. Rahman et al. [19] engineered nearly forty surfaces with varying micropillar dimensions, all with a highly wetting nanoscale coating; demonstrated CHF enhancements of up to ~2× the Zuber limit, correlating the CHF to the surface wickability. Alternative CHF enhancement mechanisms involving engineering the surface to induce microconvection and separate liquid–vapor pathways have also been implemented, as discussed in a recent survey [20].

Recently, in contrast to prior studies focused on better engineering of surface structures, Fazeli and Moghaddam [21] implemented a new approach to alter dynamics of the vapor departure and liquid return to the heater surface. In the new approach, a vapor permeable membrane constrains the boiling liquid near the heater surface while enabling rapid removal of bubbles/vapor from above the surface. A maximum CHF enhancement of close to 15× the Zuber limit was demonstrated. An analysis of the MHS performance suggested that the membrane permeability limited the CHF [21]. Here, we report development of a highly permeable membrane and a study of its impact on the MHS performance. In the following sections, first, the fundamental operating principle of the heat sink is briefly described. Then, development of the new membrane and testing of its transport characteristics as well as the CHF performance of the new MHS are discussed. Finally, the energy efficiency of the MHS is compared with other heat sinks presented in the literature.

2. Membrane-based heat sink operating principle

The operating principle of the MHS is illustrated in Fig. 1. The schematic cross-section of Fig. 1(a) depicts a hydrophobic vapor permeable membrane installed above a hydrophilic heater surface to constrain the boiling liquid pool on the heater surface. When a growing bubble reaches the membrane surface, a contact region forms between the two and rapidly expands, as seen in the side-view images (Fig. 1b) of a polydimethylsiloxane (PDMS) pool in which air bubbles are injected into the water pool capped by a nanofibrous polytetrafluoroethylene (PTFE) membrane. Forces generated as a result of this phenomenon along with the applied omnidirectional liquid pressure (P_{pool}) remove the bubble from the heater surface and discharge it from the liquid pool. As the bubble departs from the heater surface, the pool pressure delivers the liquid to the dry patch formed on the heater surface resulting in its rewetting. This new two-phase flow arrangement overcomes a key shortcoming of the pool boiling process – the hydrodynamic instability associated with the co-axial flow of vapor and liquid (i.e. K–Z model [11,12]).

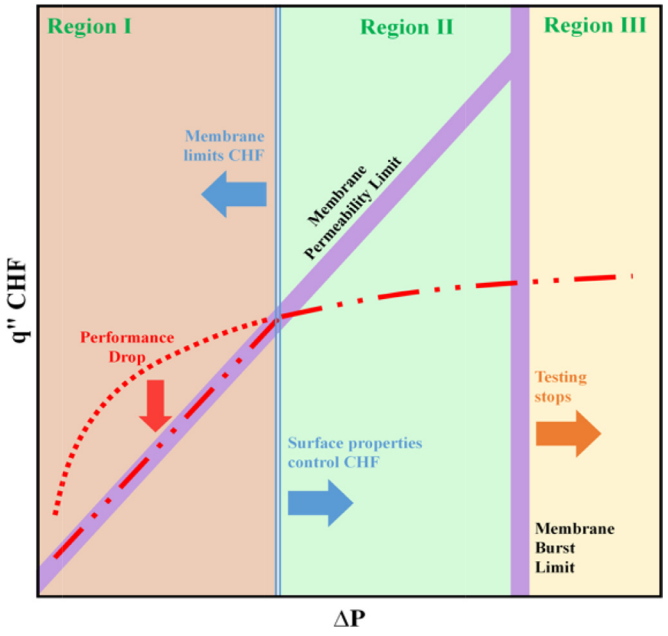

Fig. 2. An illustration showing the effect of membrane permeability on the main factors limiting the CHF depending on the pool pressure (membrane is the limiting factor at Regions I and III).

The membrane permeability and the differential pressure across it determine the rate of gas/vapor flow through the membrane [21,22], which in turn determines whether the membrane or the heater-fluid interface limit the heat flux. This phenomenon can be explained by comparing the vapor generation rate at CHF, $\dot{m}''_{CHF}(= q''_{CHF}/h_{fg})$, with the membrane mass transfer limit $\dot{m}''_{mem}$ $(= \rho_v K_{mem} \Delta P$, where K_{mem} and ρ_v are the membrane permeability and vapor density at saturation conditions, respectively). While $\dot{m}''_{CHF}$ depends on the heater-fluid interface properties, $\dot{m}''_{mem}$ is a function of membrane permeability, dictated by its geometrical characteristics (i.e. pore size, porosity, tortuosity and thickness); both are a function of $\Delta P(= P_{pool} - P_{vapor})$. If $\dot{m}''_{mem}$ is higher than $\dot{m}''_{CHF}$, CHF will not be limited by the membrane transport limit but by the heater-fluid interface (i.e. Region II shown in Fig. 2). Conversely, at low $\dot{m}''_{mem}$, it is the membrane transport limit that dictates the CHF (i.e. Region I).

Another membrane property that affects the operational range of the heat sink is the membrane breakthrough or burst pressure, which is a pressure at which the liquid is no longer constrained within the liquid pool, i.e. liquid enters the membrane pores. This dictates the upper limit of P_{pool}. The membrane breakthrough pressure is determined by the Young-Laplace equation provided below [23], where in σ is the liquid surface tension, θ is the solid–liquid contact angle, and R is the membrane pore radius.

$$\Delta P = \frac{2\sigma \mathrm{Cos}\theta}{R} \tag{1}$$

3. Experimental studies

3.1. Membrane microfabrication

A model developed to predict the MHS performance, as discussed later, suggested that in order to determine the CHF

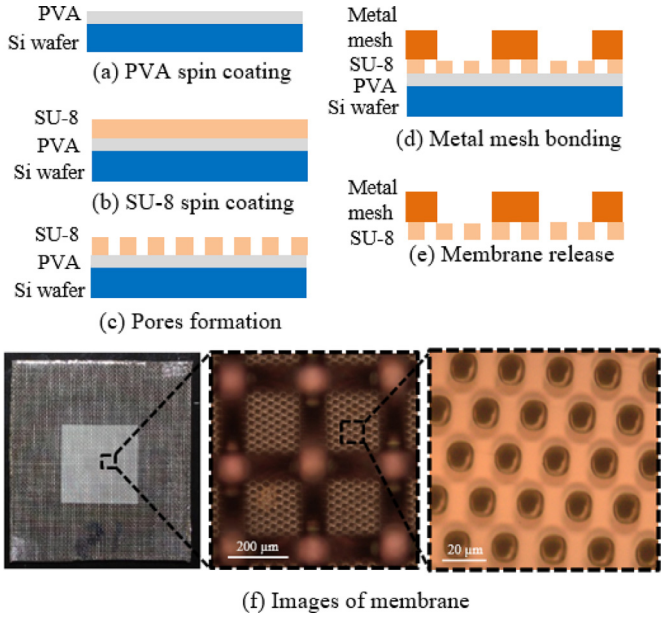

Fig. 3. Fabrication process of the bilayer SU-8 metal mesh membrane and its images.

performance of high A_r surfaces at low operating pressures (i.e. the dotted-curve in Region I of Fig. 2), a membrane with an order of magnitude higher permeability relative to the commercial membrane used in the first generation MHS is needed. Hence, our objective was to reduce the membrane thickness as much as possible. After a number of iterations, we arrived at a bilayer membrane design with an extremely thin polymer layer mechanically supported by a metal mesh with large pores with negligible pressure drop.

The polymer membrane was fabricated using SU-8 spin-on polymer solution (MicroChem Co., MA) and photolithography technique [24] and transfer-bonded on the metal mesh (TWP Inc.). Fig. 3 depicts the microfabrication sequence of the membrane. The SU-8 polymer was spin coated on a 4-μm-thick polyvinyl alcohol (PVA) sacrificial layer over a silicon (Si) wafer. The SU-8 layer was then soft baked at 95 °C and subsequently patterned using a UV light exposure unit with 1 mJ/cm^2 intensity for 80 s. The SU-8 was then developed in the SU-8 developer (MicroChem Co., MA) to form the pores. The SU-8 membrane is 8-μm-thick with ~10 μm in diameter pores spaced 10 μm apart. A stainless-steel (SS) mesh with 180 μm in diameter pores and 33% porosity (McMaster Co.) was then bonded on the SU-8 membrane. A 3-μm-thick layer of a two-component resin (Devcon HP 250) was used for this bonding process. A 3-μm-thick layer of a two-component resin was roll-coated onto the SS mesh [25]. The SU-8 and mesh layers were brought into contact and clamped between 2 glass slides, and cured in a furnace at 60 °C for 4 h. The PVA was subsequently dissolved in 90 °C de-ionized (DI) water to release the SU-8 and SS mesh assembly. Finally, the assembly was conformally coated by a 1-μm-thick Parylene film, as a moisture barrier, in a chemical vapor deposition (CVD) process (SCS Parylene coater) to prevent membrane damage in boiling water. Fig. 3(f) shows images of the final membrane.

The water contact angle (CA) of the Parylene coated membrane was 80° (Fig. 4a). To make the membrane hydrophobic, its surface was coated with hexadecyltrimethoxysilane (HDTMS) with a surface energy of 20 mN/m. The HDTMS coating increased the CA to 120° (Fig. 4b). The breakthrough pressure of the membrane was experimentally determined to be 4.9 kPa using a water column test.

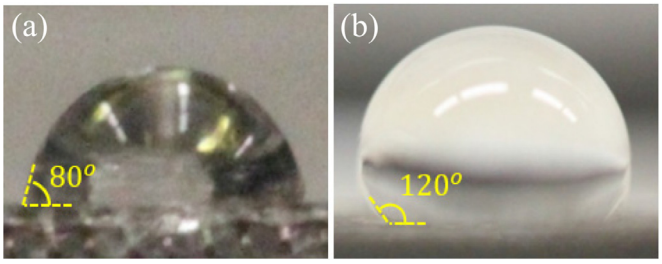

Fig. 4. Measurement of water contact angle before (a) and after (b) hexadecyltrimethoxysilane (HDTMS) coating.

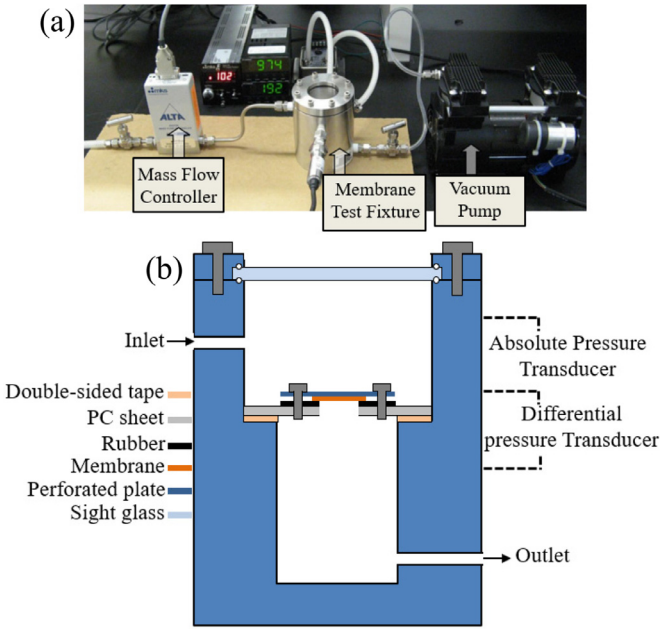

Fig. 5. (a) A photograph of the test setup for permeability measurement and (b) schematic of cross-sectional view of the test chamber.

3.2. Membrane permeability test apparatus

An experimental setup was fabricated to test the pressure drop of the membranes. A photograph of the setup is shown in Fig. 5(a). The test setup consists of a membrane test fixture, a mass flow controller (MKS instruments), a vacuum pump, absolute and differential pressure transducers, and needle valves. The vacuum pump was installed at the downstream of the test fixture to draw the test fluid through the lines.

A schematic of the membrane test fixture is shown in Fig. 5(b). The test fixture is made of Stainless Steel (SS) and consists of an upper chamber, a lower chamber, and a sight glass. Double-sided adhesive tape (3M) was used to secure the membrane on the lower chamber (cf. Fig. 5b). The test fluid enters the upper chamber, flows across the membrane into the lower chamber, and exits the lower chamber through an outlet port.

In each test, the mass flow controller was set to deliver a desired flow rate. A needle valve at the inlet of the vacuum pump was adjusted until a desired test pressure was reached in the test chamber. The absolute pressure of the upper chamber, the flow rate, and the differential pressure across the membrane were recorded.

3.3. Membrane-based heat sink (MHS) test apparatus

The heat sink is machined using a CNC in 101 copper, with an effective heated area of 0.7 × 0.7 cm^2 covered by micropillars. The

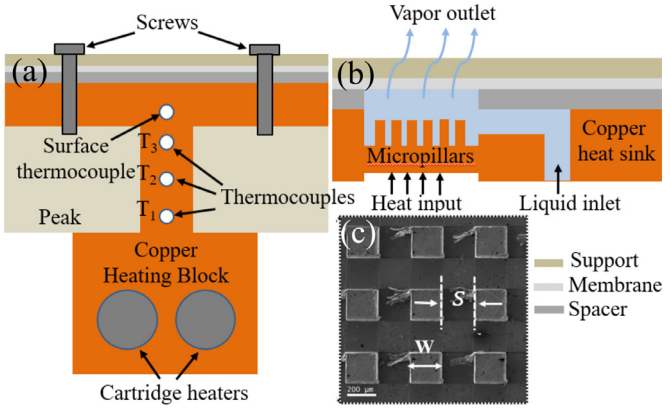

Fig. 6. (a) Cross sectional view of the setup (b) cross sectional view of the test device showing copper heat sink, silicone spacer, hydrophobic membrane, and perforated metallic support and (c) surface structures.

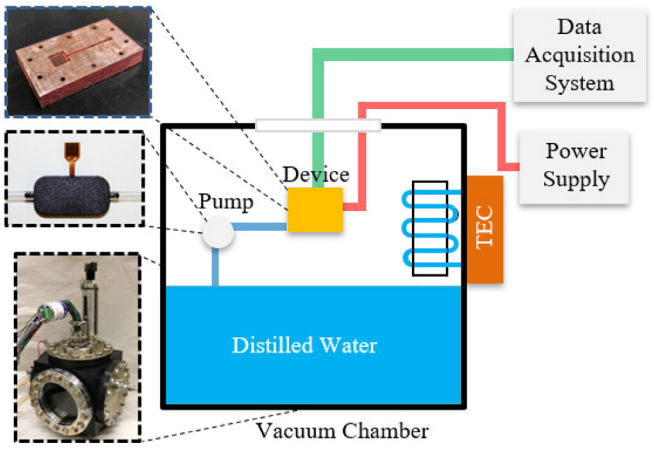

Fig. 7. Schematic of the experimental test loop.

heat sink has a liquid entry and no liquid outlet. It is brazed to a copper rode welded to a heating block. Heat is generated using 2 × 300 W cartridge heaters embedded in the heating block. The rode is encased in thermal insulation to minimize the thermal loss (Fig. 6a). Inside the test device, as depicted in the schematic of Fig. 6(b), liquid is delivered to the heated surface via a channel with a cross-section of 1 × 1 mm^2. To ensure that boiling occurs only on the structured surface, the side walls of the liquid delivery channel were covered with a 200-μm-thick layer of epoxy, since a low thermal conductivity surface is shown to inhibit boiling [26]. The liquid supply line was initially machined with a 1.2 × 1.4 mm^2 cross-section. The channel was then filled with epoxy and cured and re-machined to produce the 1.0 × 1.0 mm^2 cross-section channel. The schematic cross-section of Fig. 6(b) shows the location of surface structures and Fig. 6(c) shows their top view images. A < 1-μm-thick oxide layer was then thermally grown on the surface as described by Zhou and Yang [27] to ensure a low contact angle (CA ~ 5°) during the experiments. A 200-μm-thick rubber spacer is placed between the membrane and copper heat sink and the assembly is pressed together using a perforated metallic support.

The area ratio (A_r) of the heat sink is defined as the ratio of the extended surface area to the projected area of the heat sink, and is calculated using the following equation:

$$A_r = 1 + {}^{4wh}/_{(s+w)^2} \tag{2}$$

where w and h represent fins width and height, respectively, and s represents spacing between the fins.

Fig. 7 shows a schematic and images of the experimental test system in which the CHF measurements were conducted. The test article shown in Fig. 6 is installed in a custom-made test chamber capable of maintaining saturation conditions. Distilled water, selected as the working fluid, is delivered to the heat sink through a piezoelectric micropump (Model MP6, manufactured by Bartels Mikrotechnik GmbH). This micropump can independently control the supplied liquid pressure and flow rate by adjusting the applied voltage and frequency, respectively. Two pressure transducers are utilized to monitor the test chamber (Setra 730) and heat sink (Omega PX26) pressures. An Agilent data acquisition system is used to record the temperature and pressure data. The generated vapor leaving the test article is condensed on the chamber sidewall by a thermoelectric cooler (TEC).

The temperature readings recorded by the thermocouples (i.e. T_1, T_2, and T_3 in Fig. 6) were used to calculate the heat flux using the following equation:

$$q'' = -k\frac{dT}{dx} \sim k \times (3T_1 - 4T_2 + T_3)/2\Delta x \tag{3}$$

Table 1
Uncertainties of different variables.

Variable	Uncertainty
δT	±0.65 K
$\frac{\delta k}{k}$	±2%
$\frac{\delta \Delta x}{\Delta x}$	±0.3%
$\frac{\delta A}{A}$	0.2%
$\frac{\delta V}{V}$	±1%
$\frac{\delta \Delta P}{\Delta P}$	±0.25%

where k and Δx are the copper thermal conductivity and spacing between thermocouples, respectively. To ensure repeatability of the data, each test was conducted three times. The experimental values reported for each test is the averaged value of the three tests.

3.4. Uncertainty analysis

T-type thermocouples were used to record the temperatures. Eq. (3) is used to calculate the heat flux dissipated through the liquid phase change process. The uncertainty associated with the heat flux is due to the temperature readings, thermal conductivity of copper, and spacing between the thermocouples. The following equation was used to calculate the heat flux uncertainty:

$$\frac{\delta q''}{q''} = \left[\left(\frac{\delta k}{k}\right)^2 + \left(\frac{\delta \Delta T}{\Delta T}\right)^2 + \left(\frac{\delta \Delta x}{\Delta x}\right)^2\right]^{1/2} \tag{4}$$

where δk, $\delta \Delta T$, $\delta \Delta x$ are the thermal conductivity, temperature gradient, and space measurement uncertainties, respectively. Given that $\Delta T = 3T_1 - 4T_2 + T_3$, the $\delta \Delta T$ can be calculated using equation:

$$\delta \Delta T = \left[(3\delta T)^2 - (4\delta T)^2 + (\delta T)^2\right]^{1/2} \sim 4.12\delta T \tag{5}$$

The uncertainty associated with different experimental variables are tabulated in Table 1. The heat flux uncertainty is found to be ±13.2% at the low CHF of 180 W/cm^2 and ±7.2% at the highest CHF of 1800 W/cm^2.

The uncertainty associate with the heat transfer coefficient ($h = \frac{q}{A\Delta T_{sup}}$) is calculated using the following equation.

$$\frac{\delta h}{h} = \left[\left(\frac{\delta q}{q}\right)^2 + \left(\frac{\delta \Delta T_{sup}}{\Delta T_{sup}}\right)^2 + \left(\frac{\delta A}{A}\right)^2\right]^{1/2} \tag{6}$$

Table 2
Membranes properties.

Membrane	Average pore size (μm)	Permeability (kg/s/cm^2/kPa)
Commercial (acrylic copolymer)	12	1.8E^{-5}
Custom-made (SU-8 and metal mesh)	10	1.3E^{-4}

where ΔT_{sup} and A are the surface superheat temperature and the heater surface area, respectively. The uncertainty in h is determined to be ±33.5% at a low heat flux of 310 W/cm^2 and ±6.9% at a high heat flux of 830 W/cm^2.

Eq. (7) is used to calculate the membrane permeability.

$$p = \frac{\rho_v V}{\Delta P} \tag{7}$$

where p, V, and ΔP are the membrane permeability, gas velocity, and the differential pressure across the membrane. Therefore, the uncertainty associated with the membrane permeability is due to uncertainty in the gas velocity and differential pressure measurements, determined using the following equation:

$$\frac{\delta p}{p} = \left[\left(\frac{\delta V}{V}\right)^2 + \left(\frac{\delta \Delta P}{\Delta P}\right)^2\right]^{1/2} \tag{8}$$

The mass flow controller was calibrated by the manufacturer with an accuracy of 1% of reading. The pressure drop across the membrane was measured using a differential pressure transducer (Omega Engineering) with a range of 0–250 Pa and an accuracy of ±0.25% of the full scale. The absolute pressure in the test chamber was measured using an absolute pressure transducer (Omega Engineering) with a range of 0–108 kPa and an accuracy of 0.08%. Hence, the uncertainty in the membrane permeability is less than ±1.2%.

4. Results and discussions

4.1. Membrane permeability and impact on CHF

The permeability tests were performed on the new (custom-made) and commercial membranes. The volumetric flow rate at standard conditions as a function of pressure difference across the membrane are plotted in Fig. 8. The flow rate and pressure drop data are used to determine the membranes permeability. The results clearly show the advantage of the custom-made membrane over the commercial membrane – an increase in permeability of nearly 7 times (Table 2).

As mentioned earlier, the membrane permeability in conjunction with the pressure potential across it, i.e. $P_{pool} - P_{vapor}$ (cf. Fig. 1) are key factors limiting the CHF. Using properties of water vapor at saturation conditions (at atmospheric pressure), we have determined the heat flux equivalent of the maximum vapor mass flux through the membrane, as a function of the pressure potential across the membrane (i.e. $P_{pool} - P_{vapor}$), when implemented in the MHS. The results are provided in Fig. 9.

A model developed by Fazeli and Moghaddam [21], discussed in Section 4.3, predicts the CHF limit of the MHS. The model determines the CHF based on the surface structures and fluid properties. Dimensions of the surface structures (cf. Fig. 6c) and their wickability and surface area ratio (A_r) are listed in Table 3. Past work on defining wickability of surface structures in boiling [28] utilized a technique commonly used in the heat pipe wick literature that involves estimating the structure capillary pressure (P_c) and permeability (K_{wick}) using existing models. The liquid flux is then calculated using Darcy's law ($\dot{m}''_{wick} = \rho K_{wick} P_c / \mu L$), where ρ and μ denote liquid density and viscosity, respectively. One issue with this approach is that a wicking length is required to calculate $\dot{m}''_{wick}$. In this study, the ability of a surface to wick a liquid is simply defined as the product of its permeability and capillarity ($K_{wick}P_c$) to avoid an *ad hoc* assumption about the wicking length. This value for different surface structures is calculated (Table 3) using two models that were experimentally verified in prior studies [29–32].

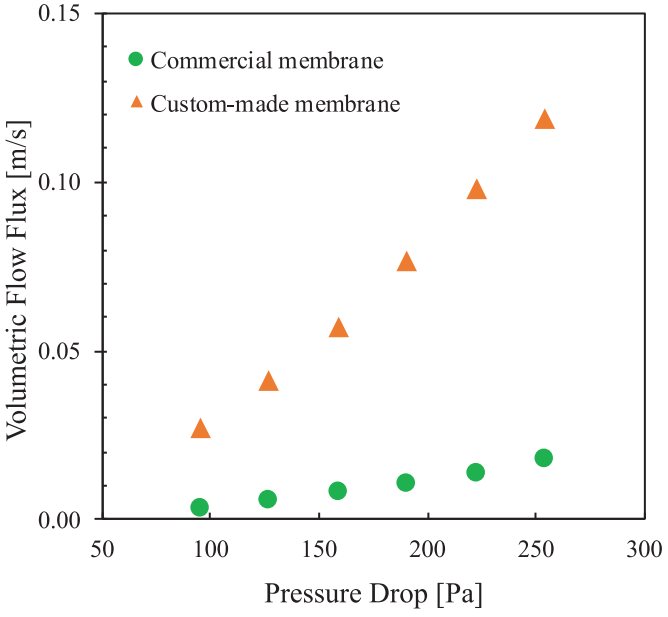

Fig. 8. Comparison of the permeability of the commercial and custom-made membranes (uncertainty is ±1%).

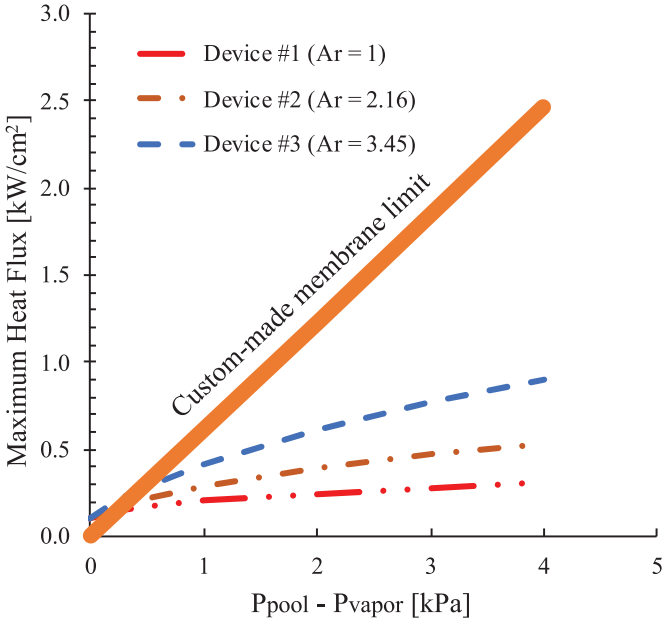

Fig. 9. Critical heat flux (CHF) estimations of different devices with the custom-made membrane.

Table 3
Geometry, wickability, and maximum CHF performance of three tested surfaces (one plain and two structured). See Fig. 6 for *S* and *W*. *H* is fin height.

Device	S (μm)	W (μm)	H (μm)	$K_{wick}P_C \times 10^6$ (Pa.m^{-2})	Area Ratio (A_r)	Max. CHF/A_r
1	N/A	N/A	N/A	N/A	1.0	505
2	300	350	350	0.754	2.16	470
3	200	150	500	0.757	3.45	510

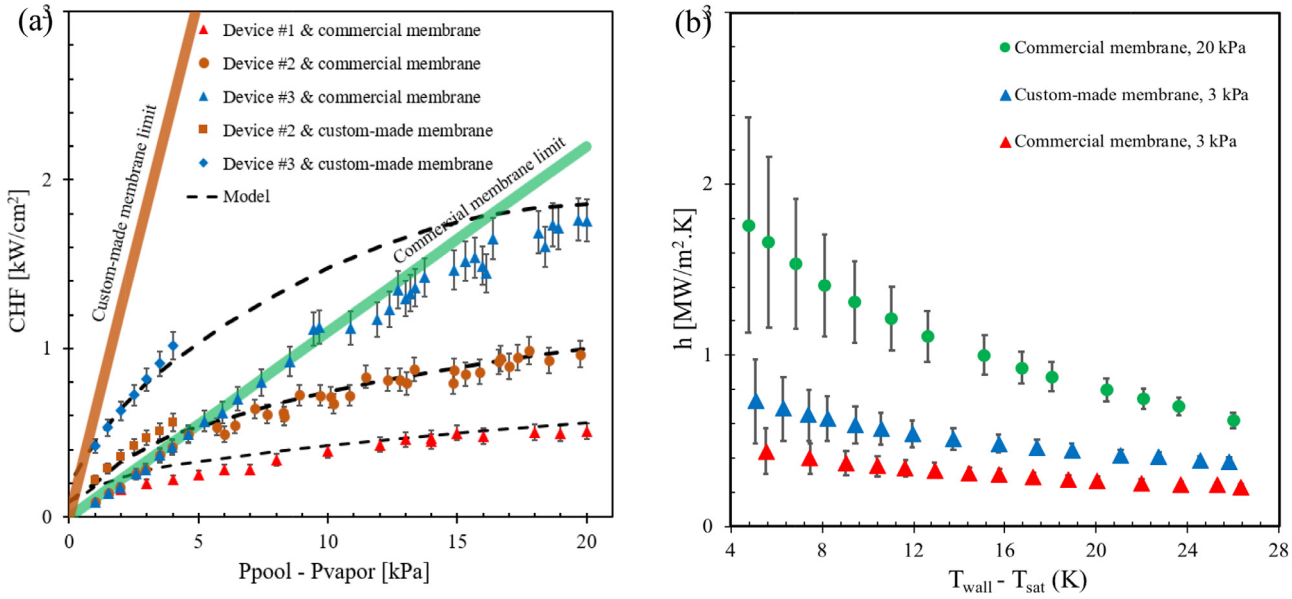

Fig. 10. (a) Critical heat flux (CHF) of different devices and comparison with model and (b) heat transfer coefficient (***h***) as a function of surface superheat temperature for Device #3.

The model's predictions for three surfaces used in this study are compared with the membrane limiting heat flux in Fig. 9. This comparison clearly suggests that the custom-made membrane does not limit the CHF, allowing the surface structures reach their maximum CHF at very low operating pressures.

4.2. Critical heat flux (CHF) test results

The MHS performance is analyzed through a set of tests conducted at different $P_{pool} - P_{vapor}$, while P_{vapor} is maintained at 100 kPa. During each experiment, at each P_{pool}, heat flux is increased incrementally until a sudden jump in the temperature is observed. The heat input at this point corresponds to the CHF at the specific $P_{pool} - P_{vapor}$. The first experimental measurement of CHF was conducted on a device with a planar heater surface (i.e. Device #1 in Table 3). Results on this device shows little difference in performance when operated with the commercial and custom-made membranes (cf. Fig. 10a). Since the commercial membrane has a significantly higher breakthrough pressure compared to the custom-made membrane, it allows for a wider operating pressure window. The results clearly suggest that the heater surface limits the performance not the membrane mass transfer resistance. Test results on Device #2 show a clear uptick in performance as a result of using the custom-made membrane. Device #3 exhibits a much more pronounced enhancement in performance – a maximum CHF of 1025 W/cm^2 at 4 kPa operating pressure, which is more than 150% higher than that of the commercial membrane.

These results further validate the hypotheses presented by Fazeli and Moghaddam [21] on the effect of surface geometrical properties on CHF performance of the MHS. The data suggest that three structures with vastly different geometries have nearly identical CHF per unit surface area of the structure (CHF/A_r), close to 500 W/cm^2 (cf. Table 3). This linear increase in CHF with the heater surface area is enabled by the increase in $P_{pool} - P_{vapor}$, which facilitates rewetting of the entire heater surface, as the bubbles/vapor columns are squeezed/removed from the heater surface (cf. Fig. 1). The plateaus observed at 20 kPa for all devices (Fig. 10) suggest that liquid has reached the entire surface area of the heater. A comparison of the wickability of these surfaces (cf. Table 3), i.e. Devices #2 and 3 with an identical wickability and Device #1 with no wickability, shows that wickability plays no role in this phenomenon. In other words, at high $P_{pool} - P_{vapor}$, forces generated at the liquid-vapor interface near the surface greatly exceed the wickability effect.

A comparison of the heat transfer coefficient (h) of Device #3 tested with the two membranes (Fig. 10b) at the same P_{pool} suggests that the higher permeability of the custom-made membrane enhances h. This suggests that when the membrane is responsible for a smaller pressure drop (i.e. a smaller fraction of $P_{pool} - P_{vapor}$), h is enhanced. It is believed that the balance of the pressure potential facilitates bubbles removal and surface rewetting leading to a higher h. The great enhancement in h at high pressures (i.e. 20 kPa) further supports this hypothesis.

4.3. Comparison with CHF model

The model considers the effect of surface structures wickability, effective heat transfer area, and liquid pressure on CHF. Our earlier [21] and current results suggested that on structures with a similar wickability, increasing the surface area almost linearly enhances the CHF limit; hence, it is expected that $q''_{CHF} \propto A_r$. The results have also proven [21] that structures with a better wickability can reach higher CHF values at low $P_{pool} - P_{vapor}$, and that the impact of wickability and A_r directly depends on $P_{pool} - P_{vapor}$. Consequently, the

Table 4
Comparison between performance of the MHS and a selected set of heat sinks from literature.

References	Heater material	Working fluid	Surface area [cm^2]	Cooling capacity [W]	$\dot{V} \times 10^6$ [m^3/s]	Exit vapor quality (%)	ΔP [kPa]	Cooling cap./ΔP [W/kPa]	PP $\times 10^3$ [W]	TP $\times 10^{-3}$
Present study	Cu	Water	0.12	502	0.2	100	4	125.5	0.8	628
Balasubramanian et al. [33]	Cu	Water	4.21	505	1.84	11	6.5	77.7	12	42.2
Qu and Siu-Ho [34]	Cu	Water	3.38	676	0.87	31	50	13.5	43.6	15.5
Yang et al. [35]	Si	Water	0.11	60.5	0.11	23	20	3.0	1.9	28.3
Miner et al. [36,37]	Cu	R-134a	0.58	284.4	3.3	33	40	7.1	120	2.1
Kalani and Kandlikar [38]	Cu	Water	1	1070	3.4	13	30	35.7	102	10.5
Palko et al. [39]	Cu	Water	1	1342	3.08	17	42	32.0	129.7	10.3
Zhu et al. [40]	Cu	Water	0.05	48	0.076	25	14.3	3.4	1.1	44.3
Li et al. [41]	Si	Water	0.1	56	0.85	24	170	0.3	144.5	3.5
Wang and Chen [42]	Alumina	Water	0.5	615	0.27	100	186	3.3	51.5	11.9
Li et al. [43]	Si	Acetone	0.56	56	0.79	17.5	125	0.4	98.7	0.6

following correlation [21] represents the additive and multiplicative impacts of wickability and heat transfer area, respectively, on CHF.

$$q''_{CHF}\left(A_{r,eff}, \Delta P, \mathcal{W}\right) \left\{q''_{N-W}\left(A_{r,eff}=1, \Delta P \sim 0, \mathcal{W} \sim 0\right) + q''_{W}\left(A_{r,eff}=1, \Delta P, \mathcal{W}\right)\right\} \times F_1\left(A_{r,eff}, \Delta P\right) \quad (9)$$

where $A_{r,\,eff}$ represents A_r while factoring in its thermal efficiency and $\mathcal{W}$ represents surface wickability. In this equation, q''_{N-W} represents CHF of a plain surface (i.e. $A_{r,eff}=1, \mathcal{W} \sim 0$) at $\Delta P \sim 0$. Therefore, its value is independent of the surface wickability and heat transfer area and can only be changed by altering the surface contact angle. q''_W, on the other hand, represents heat flux associated with the wicking process and changes with surface wickability and $P_{pool} - P_{vapor}$. Finally, F_1 denotes the effect of enhanced heat transfer area as well as the liquid pressure on the surface structure effectiveness.

Predictions of this model are compared with the experimental data in Fig. 10, showing a close agreement for all devices, when CHF is not limited by the membrane (below 5 kPa for Device #2 and 17 kPa for Device #3 with the commercial membrane). It must be reminded that the model is developed based on the surface structures and fluid properties. Hence, its prediction is accurate only below the membrane limit.

5. Comparison of MHS performance with other heat sinks

A parameter often used to evaluate performance of a heat sink is its maximum cooling capacity versus the energy used to pump the liquid through the heat sink. This is particularly important when many heat sinks are utilized in a system such as in thermal management of energy weapons wherein waste heat on the order of 100 s kW can be generated. Here, the thermal performance (TP) is defined as the ratio of the maximum heat sink cooling capacity versus the theoretical pumping power (PP) required to flow the liquid through the heat sink. Table 4 lists these performance parameters for a set of heat sinks selected from the literature, wherein the flow inlet and exit were on the sides of the heat sinks. It can be seen that TP of the MHS is 1–2 orders of magnitude higher than the other two-phase heat sinks. Evidently, an exit vapor quality of 100% and a lower pressure drop in the MHS are responsible for its superior performance.

6. Conclusions

A highly permeable membrane was developed to advance our understanding of the physics of MHS operation at the CHF working conditions. An order of magnitude higher permeability of the custom-made membrane compared to that of the commercial membrane enabled studying CHF at low liquid supply pressures. The experimental results showed that once the membrane mass transfer limit is alleviated, significant enhancement in CHF can be achieved depending on the surface heat transfer area (A_r). Comparison between CHF of a planar surface with no wickability and two structured surfaces with an identical wickability showed that the maximum CHF is a linear function of A_r. In other words, $Max.CHF/A_r$ was constant (~500 W/cm^2) for all three surfaces. A maximum CHF of 1025 W/cm^2, 2.5 times higher than the CHF of the first generation MHS, was achieved at a differential pressure of only 4 kPa. Finally, the thermal performance versus the pumping power requirement of the MHS, as a metric of energy efficiency, was compared with that of a representative set of conventional heat sinks presented in the literature. The comparison showed that the MHS energy efficiency is 1–2 orders of magnitude higher than that of other heat sinks. This superior performance is primarily due to the minimal mass flow rate (because of a 100% exit vapor quality) as well as low pressure drop of the MHS.

Declaration of Competing Interest

The authors declare that they have no known competing financial interests or personal relationships that could have appeared to influence the work reported in this paper.

Acknowledgments

This study was supported by the US National Science Foundation (NSF) under contract 1934354 with Dr. Ying Sun as the program manager. Fabrication of the devices was conducted in the Nanoscale Research Facility (NRF) at the University of Florida.

Supplementary materials

Supplementary material associated with this article can be found, in the online version, at doi:10.1016/j.ijheatmasstransfer.2020.120312.

References

[1] S. Lin, K. Banerjee, Cool chips: opportunities and implications for power and thermal management, IEEE Trans. Electron Dev. 55 (2008) 245–255, doi:10.1109/TED.2007.911763.
[2] S. Kumar, Recent progress in terahertz quantum cascade lasers, IEEE J. Sel. Top. Quantum Electron. 17 (2011) 38–47.
[3] U.K. Mishra, L. Shen, T.E. Kazior, Y. Wu, GAN-based RF power devices and amplifiers, Proc. IEEE 96 (2008) 287–305, doi:10.1109/JPROC.2007.911060.
[4] S.V Garimella, A.S. Fleischer, J.Y. Murthy, A. Keshavarzi, R. Prasher, C. Patel, S.H. Bhavnani, R. Venkatasubramanian, R. Mahajan, Y. Joshi, B. Sammakia, B.A. Myers, L. Chorosinski, M. Baelmans, P. Sathyamurthy, P.E. Raad, Thermal challenges in next-generation electronic systems, IEEE Trans. Components Packag. Technol. 31 (2008) 801–815, doi:10.1109/TCAPT.2008.2001197.

[5] S. Moghaddam, K.T. Kiger, Microscale Study of the Boiling Process in Low-Surface-Tension Fluids, (2006).
[6] S. Moghaddam, K. Kiger, Physical mechanisms of heat transfer during single bubble nucleate boiling of FC-72 under saturation conditions-I. Experimental investigation, Int. J. Heat Mass Transf. 52 (2009) 1284–1294.
[7] S. Nukiyama, The maximum and minimum values of the heat Q transmitted from metal to boiling water under atmospheric pressure, Int. J. Heat Mass Transf. 9 (1934) 1419–1433, doi:10.1016/0017-9310(66)90138-4.
[8] M.T. Cichelli, C.F. Bonilla, Heat transfer to liquids boiling under pressure, Trans. Am. Soc. Chem. Eng. 41 (1945) 755–787.
[9] C.F. Bonilla, C.W. Perry, Heat transmission to boiling binary liquid mixtures, Trans. Am. Soc. Chem. Eng. 37 (1941) 685–705.
[10] W.M. Rohsenow, P. Griffith, Correlation of Maximum Heat Flux Data for Boiling of Saturated Liquids. Technical Report No. 6, 1955.
[11] N. Zuber, Hydrodynamic Aspects of Boiling Heat Transfer, 196, University of California, 1959, doi:10.2172/4175511.
[12] S.S. Kutateladze, On the transition to film boiling under natural convection, Kotloturbostroenie 3 (1948) 10.
[13] D. Attinger, C. Frankiewicz, A.R. Betz, T.M. Schutzius, R. Ganguly, A. Das, C.-J. Kim, C.M. Megaridis, Surface engineering for phase change heat transfer: A review, MRS Energy Sustain. 1 (2014) E4, doi:10.1557/mre.2014.9.
[14] R. Moissis, P.J. Berenson, On the hydrodynamic transitions in nucleate boiling, J. Heat Transf. 85 (1963) 221–226, doi:10.1115/1.3686075.
[15] T.D. Bui, V.K. Dhir, Transition boiling heat transfer on a vertical surface, J. Heat Transf. 107 (1985) 756–763, doi:10.1115/1.3247501.
[16] H. Jo, H.S. Ahn, S. Kang, M.H. Kim, A study of nucleate boiling heat transfer on hydrophilic, hydrophobic and heterogeneous wetting surfaces, Int. J. Heat Mass Transf. 54 (2011) 5643–5652, doi:10.1016/J.IJHEATMASSTRANSFER.2011.06.001.
[17] S.G. Kandlikar, A theoretical model to predict pool boiling CHF incorporating effects of contact angle and orientation, J. Heat Transf. 123 (2001) 1071–1079, doi:10.1115/1.1409265.
[18] H.S. Ahn, H.J. Jo, S.H. Kang, M.H. Kim, Effect of liquid spreading due to nano/microstructures on the critical heat flux during pool boiling, Appl. Phys. Lett. 98 (2011) 071908, doi:10.1063/1.3555430.
[19] M.M. Rahman, E. Ölçeroğlu, M. McCarthy, Role of wickability on the critical heat flux of structured superhydrophilic surfaces, Langmuir 30 (2014) 11225–11234.
[20] S.G. Kandlikar, Enhanced macroconvection mechanism with separate liquid–vapor pathways to improve pool boiling performance, J. Heat Transf. 139 (2017), doi:10.1115/1.4035247.
[21] A. Fazeli, S. Moghaddam, A new paradigm for understanding and enhancing the critical heat flux (CHF) limit, Sci. Rep. 7 (2017) 5184, doi:10.1038/s41598-017-05036-2.
[22] A. Fazeli, M. Mortazavi, S. Moghaddam, Hierarchical biphilic micro/nanostructures for a new generation phase-change heat sink, Appl. Therm. Eng. 78 (2015) 380–386, doi:10.1016/j.applthermaleng.2014.12.073.
[23] A.R. Kovscek, C.J. Radke, Gas bubble snap-off under pressure-driven flow in constricted noncircular capillaries, Colloids Surf. A Physicochem. Eng. Asp. 117 (1996) 55–76, doi:10.1016/0927-7757(96)03637-0.
[24] L. Amato, S.S. Keller, A. Heiskanen, M. Dimaki, J. Emnéus, A. Boisen, M. Tenje, Fabrication of high-aspect ratio SU-8 micropillar arrays, Microelectron. Eng. 98 (2012) 483–487, doi:10.1016/j.mee.2012.07.092.
[25] M. Mortazavi, A. Fazeli, S. Moghaddam, Scalable bonding of nanofibrous polytetrafluoroethylene (PTFE) membranes on microstructures, J. Micromech. Microeng. 28 (2018) aa8185, doi:10.1088/1361-6439/aa8185.
[26] M.M. Rahman, J. Pollack, M. McCarthy, Increasing boiling heat transfer using low conductivity materials, Sci. Rep. 5 (2015) 13145, doi:10.1038/srep13145.
[27] G. Zhou, J.C. Yang, Temperature effect on the Cu_2O oxide morphology created by oxidation of Cu(0 0 1) as investigated by in situ UHV TEM, Appl. Surf. Sci. 210 (2003) 165–170, doi:10.1016/S0169-4332(03)00159-4.
[28] N.S. Dhillon, J. Buongiorno, K.K. Varanasi, Critical heat flux maxima during boiling crisis on textured surfaces, Nat. Commun. 6 (2015) 8247.
[29] A. Tamayol, M. Bahrami, Transverse permeability of fibrous porous media, Phys. Rev. E 83 (2011) 46314, doi:10.1103/PhysRevE.83.046314.
[30] C. Byon, S.J. Kim, The effect of meniscus on the permeability of micro-post arrays, J. Micromech. Microeng. 21 (2011) 115011.
[31] R. Xiao, R. Enright, E.N. Wang, Prediction and optimization of liquid propagation in micropillar arrays, Langmuir 26 (2010) 15070–15075, doi:10.1021/la102645u.
[32] S. Ravi, D. Horner, S. Moghaddam, Monoporous micropillar wick structures, I-Mass transport characteristics, Appl. Therm. Eng. 73 (2014) 1371–1377, doi:10.1016/j.applthermaleng.2014.04.057.
[33] K. Balasubramanian, P.S. Lee, L.W. Jin, S.K. Chou, C.J. Teo, S. Gao, Experimental investigations of flow boiling heat transfer and pressure drop in straight and expanding microchannels – A comparative study, Int. J. Therm. Sci. 50 (2011) 2413–2421, doi:10.1016/j.ijthermalsci.2011.07.007.
[34] W. Qu, A. Siu-Ho, Experimental study of saturated flow boiling heat transfer in an array of staggered micro-pin-fins, Int. J. Heat Mass Transf. 52 (2009) 1853–1863, doi:10.1016/j.ijheatmasstransfer.2008.10.008.
[35] F. Yang, X. Dai, Y. Peles, P. Cheng, J. Khan, C. Li, Flow boiling phenomena in a single annular flow regime in microchannels (II): Reduced pressure drop and enhanced critical heat flux, Int. J. Heat Mass Transf. 68 (2014) 716–724, doi:10.1016/j.ijheatmasstransfer.2013.09.060.
[36] M.J. Miner, P.E. Phelan, B.A. Odom, C.A. Ortiz, Experimental measurements of critical heat flux in expanding microchannel arrays, J. Heat Transf. 135 (2013) 1–8, doi:10.1115/1.4024388.
[37] M.J. Miner, P.E. Phelan, B.A. Odom, C.A. Ortiz, An experimental investigation of pressure drop in expanding microchannel arrays, J. Heat Transf. 136 (2014) 1–9, doi:10.1115/1.4025557.
[38] A. Kalani, S.G. Kandlikar, Heat Dissipation Beyond 1 kW/cm2 With Low Pressure Drop and High Heat Transfer Coefficient for Flow Boiling Using Open Microchannels With Tapered Manifold, (2016). https://doi.org/10.1115/ICNMM2016-7918.
[39] J.W. Palko, H. Lee, D.D. Agonafer, C. Zhang, K.W. Jung, J. Moss, J.D. Wilbur, T.J. Dusseault, M.T. Barako, F. Houshmand, G. Rong, T. Maitra, C. Gorle, Y. Won, D. Rockosi, I. Mykyta, D. Resler, D. Altman, M. Asheghi, J.G. Santiago, K.E. Goodson, High heat flux two-phase cooling of electronics with integrated diamond/porous copper heat sinks and microfluidic coolant supply, in: Proceedings of the 15th Intersociety Conference on Thermal and Thermomechanical Phenomena in Electronic Systems (ITherm 2016), 2016, pp. 1511–1517, doi:10.1109/ITHERM.2016.7517728.
[40] Y. Zhu, D.S. Antao, K.H. Chu, S. Chen, T.J. Hendricks, T. Zhang, E.N. Wang, Surface structure enhanced microchannel flow boiling, J. Heat Transf. 138 (2016) 1–13, doi:10.1115/1.4033497.
[41] W. Li, X. Qu, T. Alam, F. Yang, W. Chang, J. Khan, C. Li, Enhanced flow boiling in microchannels through integrating multiple micro-nozzles and reentry microcavities, Appl. Phys. Lett. 110 (2017) 1–5.
[42] Q. Wang, R. Chen, Ultrahigh flux thin film boiling heat transfer through nanoporous membranes, Nano Lett. 18 (2018) 3096–3103.
[43] Y.F. Li, G.D. Xia, D.D. Ma, J.L. Yang, W. Li, Experimental investigation of flow boiling characteristics in microchannel with triangular cavities and rectangular fins, Int. J. Heat Mass Transf. 148 (2020) 1–18.